POAC'13
Espoo, Finland

Proceedings of the 22nd International Conference on
Port and Ocean Engineering under Arctic Conditions
June 9-13, 2013
Espoo, Finland

Modelling oil entrapment in sea ice on the basis of 3d micro-tomographic images

Sönke Maus[1], Sabine Leisinger[2], Margret Matzl[2], Martin Schneebeli [2] and Andreas Wiegmann[3]

[1]Geophysical Institute, University of Bergen, NORWAY, email: sonke.maus@gfi.uib.no,[2]WSL Swiss Federal Institute for Snow and Avalanche Research, Davos, SWITZERLAND, [3]Math2Market GmbH, Kaiserslautern, GERMANY

ABSTRACT

Oil entrapment in drifting sea ice may lead to release of oil far away from spilling locations, when the ice finally melts at the end of its drift. The entrapment process hence needs to be understood properly to evaluate the environmental risks of oil spills in ice-covered waters. However, field studies of oil-in-ice processes are sparse, while laboratory tests do not necessarily represent natural sea ice in terms of growth conditions, time scales and, in particular, microstructures. In this study we consider the role that the microstructure of sea ice may play for oil entrapment. We discuss oil migration into the sea ice pore space on the basis of 3-d images of young winter sea ice, obtained by X-ray micro-tomography. Simulating fluid flow through these images we obtain the vertical distribution of sea ice permeability and pore size distributions, the basic parameter for the prediction of migration of oil into the ice. We compare the analysis with published results from laboratory experiments of oil entrapment in laboratory-grown ice of similar age. Our analysis suggests that care must be taken when interpreting laboratory experiments, due to limited oil amounts released. Furthermore, we perform a similar analysis of older and thicker summer ice that has similar porosity yet coarser pores. The potential of the old ice to entrap oil is expected to be an order of magnitude larger than indicated by results with young laboratory-grown ice. Due to the importance of sea ice microstructure to predict oil entrapment and transport, future approaches should include models of sea ice microstructure evolution with growth and melt conditions.

INTRODUCTION

The interest in Arctic oil deposits is presently increasing, as the ongoing climate change implies easier accessibility of the region (e.g., Rogers et al., 2013). To evaluate the environmental risks of oil exploration in these ice-covered areas, oil-ice interaction has to be properly understood. Of particular interest is the situation of an oil spill in completely ice covered areas. Experiments with controlled oil spills in the field and laboratory (Wolfe and Hoult, 1974; Martin, 1979; Fingas and Hollebone, 2003; Otsuka et al., 2004; Karlsson, 2009; Dickins, 2011) indicate that oil released during the growth season of first-year ice will (i) be encapsulated as a layer in the growing ice sheet, and (ii) likely be released during the next melt season. In cases where the ice warms and melts internally, the oil has been observed to migrate to its surface through brine channels. To predict this timing of oil migration and surface release, is apparently important for logistics of clean-up, and evaluation of areas affected during ice drift (of typically hundreds of kilometers per month). An important question in this context is to what proportions oil remains in topographic depressions below the ice, or may migrate into the sea ice pore space and be eventually released from there. The migration process is however not well understood, both due to a lack in field

observations, and due to incomplete knowledge of sea ice microstructure evolution during melt and growth.

Recently, several laboratory experiments have been performed on the migration of oil into sea ice (Otsuka et al., 2004; Karlsson, 2009):
(I) Otsuka et al. (2004) released oil corresponding to an equivalent layer thickness of 3 and 8 mm to the bottom of 15 cm thick laboratory-grown seawater ice. Ice growth was continued below this encapsulated oil layer, and oil porosities were measured about 10 days later. Within 5 cm of the its release level, the oil was found to occupy up to half of the pore space; at distances 5 to 10 cm this fraction dropped to below 10%. The authors concluded that trapped oil can migrate into sea ice also during the freezing season.
(II) Karlsson (2009) performed similar release experiments under 10 to 15 cm laboratory-grown seawater ice. The released equivalent oil layer thicknesses were smaller, from 0.5 to 4 mm. During experiments with growing ice the oil did not migrate farther then 2-3 cm from the bottom of the ice, where it occupied up to two thirds of the pore space. During warming/ melting experiments the oil was distributed through the whole ice, yet only occupied roughly 5% of the pore space. Oil was observed to reach the surface in pores of 1-2 mm diameter.

Based on these studies, Karlsson et al. (2011) suggested an oil uptake capacity of $\approx$ 1 l/m^2 during the sea ice growth season, and proposed that oil migration is limited by a threshold porosity of 0.10 to 0.15, to the near bottom layers. Petrich et al. (2013) extended the work by a macroscopic modelling study of oil migration. They assumed (i) a porosity threshold of 0.1 to 0.15, such that oil entrainment may occur, as well as, on the basis of field work results from NORCOR (1975), (ii) a limiting oil fraction of 4.5 % by weight, irrespective of the total porosity of the ice in case of oil migration. With this approach they estimated, for average climate conditions near Barrow, Alaska, a larger uptake of 5 to 10 l/m^2 and a penetration depth of crude oil into sea ice of 0.1 to 0.2 m by the end of the growth season. Petrich et al. (2013) concluded that this storage capacity is roughly 20% of the under-ice storage of typically that 10 to 60 l/m^2 (Fingas and Hollebone, 2003).

None of the above studies included quantitative observations and analyses of the sea ice microstructure through which the oil flow takes place. Also, due to the short duration of laboratory experiments of typically a week, it is an open question if the results can be used for longer time predictions, when the microstructure and potential for oil migration might change significantly. Last but not least, the amounts of oil released in laboratory studies were limited to a few millimeters, and might not reflect the potential in the field. In the present paper we analyse recently obtained 3-d observations of the microstructure of sea ice in terms of the oil uptake capacity, compare them with results from the mentioned laboratory studies., and address these aspects critically.

FIELD WORK AND METHODS

Sea ice samples for the present study were obtained from fast ice in Adventbay of Adventfjorden, Svalbard during 14^{th} to 19^{th} April 2011 (Figures 1 and 2). Sampling was performed three times at the same site in the middle of the bay, approximately 2 km from the UNIS (University Courses on Svalbard) building. During each sampling 6 full ice cores were obtained with a 7.25 cm diameter coring device (Mark III, Kovacs Enterprises) from 35 cm thick fast ice. Cores were immediately cut into 3-4 cm thick subsamples. On a first ice core, temperatures were measured with a penetration probe - this core was not used further. All other cores were packed into conical lockable plastic beakers and stored in an isolating box. They were then rapidly (by snow mobiles, within 30 minutes from the beginning of coring) transported to the UNIS laboratory, where they were stored in temperature-controlled freezers (WAECO Coolfreeze T56) close to their *in situ* temperatures (typically within 0.3 K).

In a laboratory at UNIS the samples were, after maximum 1-2 days of storage, centrifuged at their respective temperatures in a refrigerated centrifuge of type Sigma 6K15. As the samples were relatively warm and soft, a value of 15 $\times g$ (earth gravity) was selected for centrifuging. This ensures a pressure force smaller than 15 kPa, below the lowest tensile strength values (20-50 kPa)

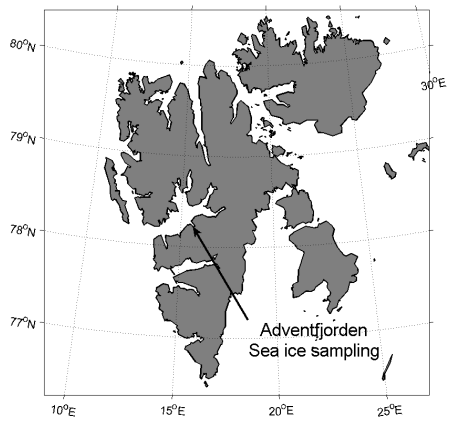

Figure 1: Sampling site Adventbay in Adventfjorden/Svalbard.

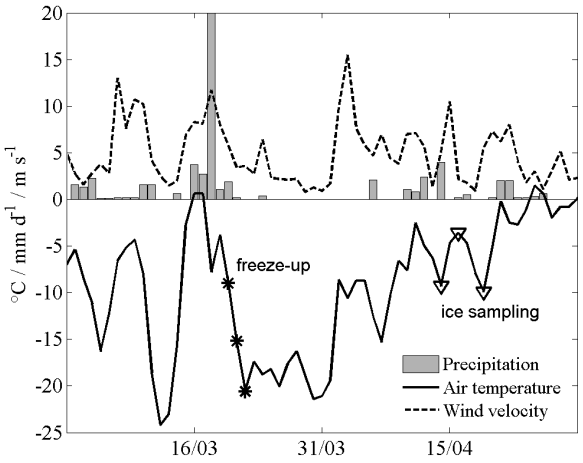

Figure 2: Meteorological conditions at Longyearbyen airport, from freeze-up to sampling three to four weeks later.

observed for natural sea ice (Weeks, 2010). In our protocol the subsamples are placed on the field site into conical boxes, which also collects the brine that drained from them prior to centrifuging. Immediately after centrifugation the ice samples were stored in a -80 °C low temperature freezer, and the mass of centrifuged brine and residual ice samples measured. The centrifuged samples were then reduced from the initial 7.25 cm to 4 cm diameter, and the ice that was cut off was melted. The centrifuged brine and melted residual ice were filtered with a 100 μm sieve, then the salinity was determined via measurements of the electrolytic conductivity and temperature (instrument WTW Cond 340i). Brine samples with salinity > 40g/kg were diluted to perform the conductivity-salinity conversion with seawater standard formulas. Salinity values obtained in this way have an accuracy of better than 0.2 g/kg.

Central to our approach was to centrifuge brine from sea ice samples at different temperatures. That is, after one core had been processed at *in situ* temperatures, we repeated the procedure for the replicates, lowering the temperature gradually below the in situ values (mostly in the range -2 to -3 °C) down to -10 °C. These cooled samples were then treated and analysed in the same way. All centrifuged ice samples were later, in order to minimise their metamorphosis by diffusion, kept at -80 °C, until imaging by X-ray micro computed tomography (XRT) described below. As noted below, centrifuging is a necessary prerequisite for absorption-based tomographic imaging of sea ice samples, because the low absorption contrast of brine and ice does not yield good quality images of pore networks. However, replacing the interconnected brine by air makes not only XRT imaging of the emptied pore networks possible, - it also makes microstructure changes during storage much less a problem. Last but not least, the centrifuging approach gives useful macroscopic information about the sea ice samples, as it provides (i) the hydrodynamically accessible brine/salt fraction and (ii) the fraction of brine that is either hardly extractable or disconnected. Let the total brine porosity ϕ be the sum of the centrifuged brine porosity ϕ_d and the residual brine porosity ϕ_r. Then, assuming that the corresponding brine salinities are the same, these porosities may be determined from salinity determinations alone. The centrifuged brine porosity is given as

$$\phi_d = 1 - \phi \frac{S_{ir}}{S_i} \left(\frac{S_b - S_i}{S_b - S_{ir}} \right), \tag{1}$$

where S_i is the bulk salinity of the original ice sample, S_{ir} the residual salinity of a sample after centrifugation and S_b the salinity of the centrifuged brine, and ϕ was determined from S_i and temperature T_i, assuming thermodynamic equilibrium and applying equations from Cox and Weeks (1983).[1]

[1] Alternatively ϕ_d and ϕ_r can be computed from the mass and salinity of the centrifuged brine and ice samples, see Weissenberger et al. (1992), who presented the results in terms of the ratio ϕ_r/ϕ.

In addition to the detailed young ice data, we also we present some analysis of samples from the center (ca 0.4 m from the bottom) of 1.0 m thick summer first-year ice, obtained at the end of the melting season during a cruise into the Marginal Ice Zone north of Svalbard (ICE cruise, 16.08-2.09.2010, R/V LANCE). Samples have been prepared (storage, centrifuge) in the same way prior to X-ray analysis.

MACROSCOPIC SEA ICE DESCRIPTION

The meteorological conditions in Figure 2 indicate, in combination with daily ice charts from the Ice service of the Norwegian Meteorological Institute (ftp.met.no/pub/icecharts/, not shown), that the ice in Adventbay was approximately 3-4 weeks old. After, most likely, freeze-up during 20.-22.04.2011, it mostly grew during a period of 10 days with temperatures around -20 °C, followed by 10 days with gradual warming. A 10 cm cover of new snow on the ice had mostly accumulated a few days prior to sampling. The ice thickness (35 cm on average) did not change measurably during our sampling period, the thickness range was 33 to 36 cm for the 18 cores obtained. Here we focus on the cores obtained on 16.04., when the ice was warmest, with a surface (ice-snow interface) temperature of -2.9 °C and a near bottom interface near the freezing point of seawater (-1.9 °C), see Figure 3a. The salinity of the ice was obtained from mass and salt balance of the centrifuged brine and the cut residual ice samples. It shows a classical C-shape profile (Figure 3a), with some indication of drainage at the very surface above the freeboard [2]. All 5 salinity profiles are very similar and show little variability, and so do the brine porosity profiles that span the range 0.1 to 0.2 (Figure 3b). This gives some confidence that temperature dependence, not internal variability of the cores, will dominate the results. The temperatures and brine porosity of the samples during storage/centrifuging are shown in Figure 4.

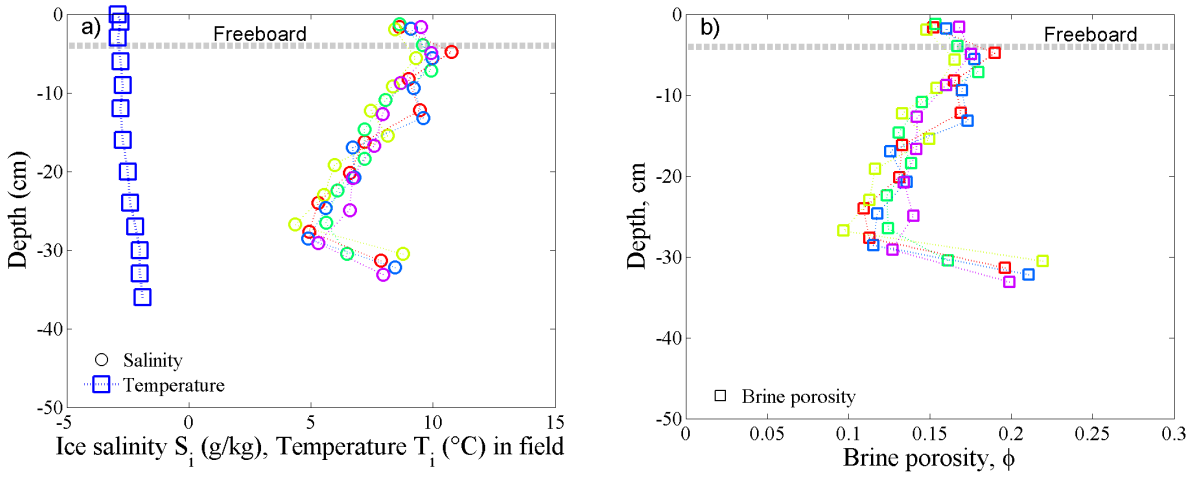

Figure 3: Core profile properties of 35 cm thick sea ice obtained on 16.03.2011 in Adventbay, Svalbard. a) In situ temperature T_i and bulk salinity S_i profiles, b) Brine porosity ϕ, from thermodynamic equilibrium based on T_i and S_i. 5 profiles are shown in different colors. The theoretical freeboard of the ice prior to snow accumulation is indicated.

In Figure 8 the centrifuged brine porosity ϕ_d obtained in the centrifuge experiment is shown in dependence on the total brine porosity ϕ. Interestingly, this figure may be taken as an indication of a threshold in ϕ at which $\phi_d = 0$, i.e. the total porosity at which no brine can be extracted from the ice. A linear fit to the data gives a value of $\phi(\phi_d = 0) = 0.011$. This value should be interpreted with care as there are no observations below $\phi = 0.04$, and the data indicate some nonlinear tendency. However, the results indicate a lack in a threshold of 0.05 for ϕ, as frequently assumed for the permeability of sea ice since suggested by Golden et al. (1998, 2007). This issue is addressed further in the next sections on the basis of permeability calculations.

[2]Note that, what is indicated as 'freeboard' in the figure, refers to the ice without the freshly fallen snow

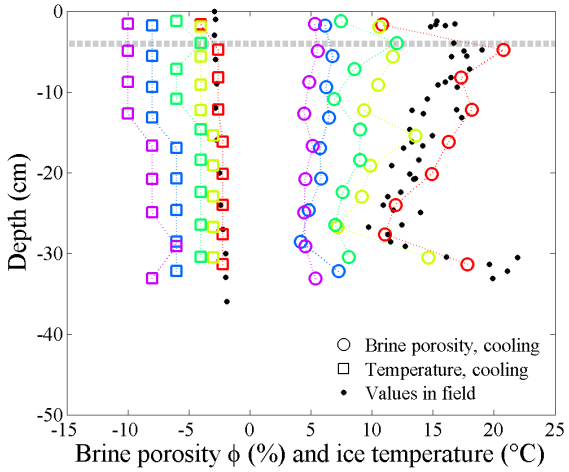

Figure 4: Temperature and brine volume during the storage/centrifugation cooling sequence. The *in situ* values are shown as small black dots. The core with realised temperatures closest to *in situ* is shown with red symbols (warmest).

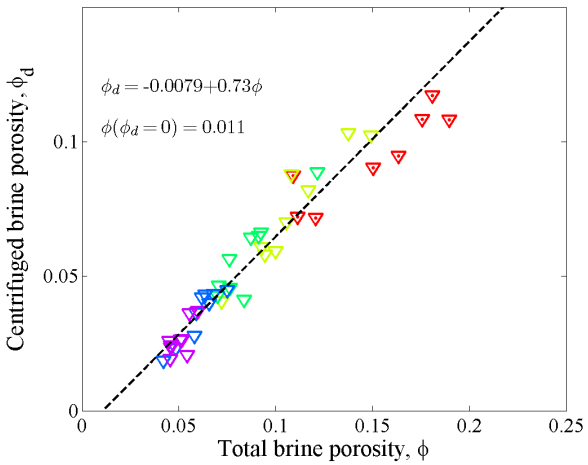

Figure 5: Relationship between centrifuged brine porosity ϕ_d and total brine porosity ϕ, different cores distinguished with same colors as in figure 4.

MICROTOMOGRAPHIC IMAGING AND PROCESSING

Most of the present knowledge of sea ice pore structure is still based on two-dimensional thin sections (e.g., Weeks, 2010). Besides their destructive nature, they were lacking 3-d information. While an early application of non-destructive X-ray 3d tomography (XRT) by Kawamura (1988) was resolution-limited to millimeter-sized pores, the technique is now available with much higher resolution. XRT with voxel size $20 - 40$ μm has been successfully applied to study the 3-d pore space of polar firn and snow (e.g., Freitag et al., 2004; Schneebeli and Sokratov, 2004). For sea ice the situation is more difficult, as the absorption contrast between brine and ice is, in contrast to air-ice for snow, insufficient to obtain good quality images of the pore space. Hence, (Golden et al., 2007) added a contrast agent to obtain images of laboratory ice grown from NaCl solution. To what degree such ice represents natural sea ice is uncertain, in particular due to different growth conditions, convection and desalination of laboratory ice, that all affect its pore microstructure.

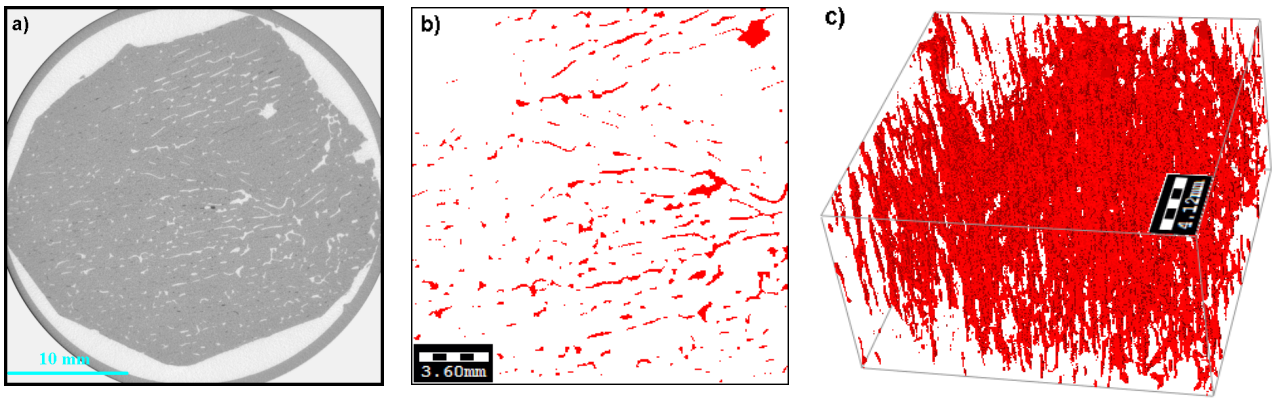

Figure 6: a) X-ray Absorption tomography slice of centrifuged young sea ice, horizontal plane (obtained at -20 °C). Ice appears grey, air (centrifuged brine) bright, and salt crystals dark. b) Cropped fraction of a), segmented into air (red) and ice (white). Right: 3d image based on 600 slices, showing the vertical curtain-like structure of brine networks.

Our approach, circumventing the problem by centrifuging prior to X-ray imaging, was tested at different resolutions (down to 1 μm) with synchrotron-based X-ray tomography (Maus et al., 2009, 2011). For the present data we performed XRT at the WSL Swiss Federal Institute for Snow

and Avalanche Research, Davos, Switzerland, with two desktop cone-beam microCT instruments (MicroCT 40 and MicroCT 80, Scanco Medical AG) that operate with a microfocus X-ray source (7 μm diameter) and detectors of 2048 x 256 and 2048 x 128 elements, respectively. Samples were scanned with a 37 mm field of view, yielding a nominal resolution of 18 μm - the voxel size at which all 3-d images were obtained. As the samples were scanned with 500 images per 180 degrees rotation, the actual resolution was probably a factor of 1.5 worse. Scanning time was roughly 1 hour per centimeter sample height. Scanning at temperatures below -23 °C would have been desirable, because much of the non-centrifugable, residual brine then transforms to solid salt and may be easily seen in absorption contrast (whereas ice and brine cannot be distinguished). However, operational problems increase with such low temperatures, and imaging was thus performed at -20 °C. Also at -20 °C we observe high absorption structures, likely related to Na_2SO_4 $10H_2O$ (mirabilite) that precipitates at temperatures below -7 to -8 °C (e.g., Maus et al., 2011), see Figure 6a. For the present analysis of permeability issues the disconnected brine pores are of minor importance and they were ignored in the following steps.

The resulting XRT grayscale images were stored as 16-bit stacks and further processed. First, the ImageJ software (rsb.info.nih.gov/ij/) was used for filtering (2 pixel median and Gaussian blur with standard deviation of 1.5) and determination of a global threshold that separates air and ice. The threshold was found on sub-images with approximately equal fractions of air pores and ice, using by Otsu's (Otsu, 1979) method. A constant value was then used to segment the whole dataset into air and ice (the latter including non-centrifuged salt and brine). From the raw image including the sample holder, a cylinder with largest possible square cross section (see Figure 6b) was cut, to obtain vertical rectangular cylinders with 2 cm length on a side and 2-2.5 cm in height. For pore space analysis and numerical computations with GeoDict (2012), "Geometric Material Models and Computational PreDictions of Material Properties", these cylinders were again subdivided vertically into samples of 5.5 mm height each. This had the advantage that permeability computations could be performed with low cost personal computers (4 cores, 32 GB Ram). Also, it gives more reliable results in terms of permeability, as for 20 mm high samples a considerable fraction (10-30%) of slightly inclined pores was running of at the sides. A segmented 3-d image (two times in height of the described basic size) is shown in Figure 6, left image.

PORE SPACE AND PERMEABILITY

A pore size distribution was obtained for each sample with by fitting spheres of increasing diameter into the pores, and thereby determining the respective volume fractions of each size class. Results for three samples of different porosities (20, 16 and 5%) are shown in Figure 7. In this figure, the 50th percentile pore diameter D_{50} (median) and the diameter that distinguishes the largest 10% of the pore space (D_{10}) are indicated as vertical lines. These values are a standard output in GeoDict and determined for all samples, to be discussed below.

Vertical permeability computations have been performed with a Stokes-solver in GeoDict, by using a thin inflow region at the top and bottom of the sample. Computations required typically 25-30 GB Ram and were performed on 4 and 8 core personal computers. Limiting the accuracy to 0.01 appeared to be sufficient for most samples to converge in between 200 to 600 iterations, which took typically 1 to 3 days per sample on a 4 core pc with a 3 GHz cpu. In total simulations were performed for about 150 samples of 5.5 mm height.

For each set of 4 to 5 serial 5.5 mm samples (representing an original 3-4 cm slice from the 35 cm sea ice cores), the permeability was then obtained as the geometric mean of the subsample permeabilities. The results are shown in Figure 8 in relation to the total brine porosity[3]. A linear log-log fit then gave an equation for the vertical permeability K:

$$K = 1.17 \times 10^{-8} \phi^{2.63} \ \ (m^2) \tag{2}$$

[3]Note that, while total ϕ and centrifuged ϕ_d were determined for macroscopic field samples, for the smaller XRT samples we only image ϕ'_d, not ϕ. We then assumed $\phi'_d = \phi_d$ and derived ϕ from the linear fit in Figure 8.

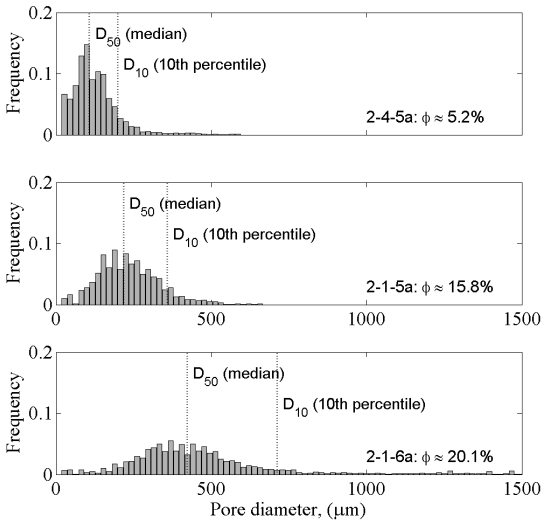

Figure 7: Pore size distribution of three subsamples, with the 50th percentile pore diameter D_{50} (median) and the diameter D_{10} (largest 10% of pores to the right) indicated as vertical lines. Samples with higher porosity ϕ are from the core 2-1 centrifuged at *in situ* temperatures.

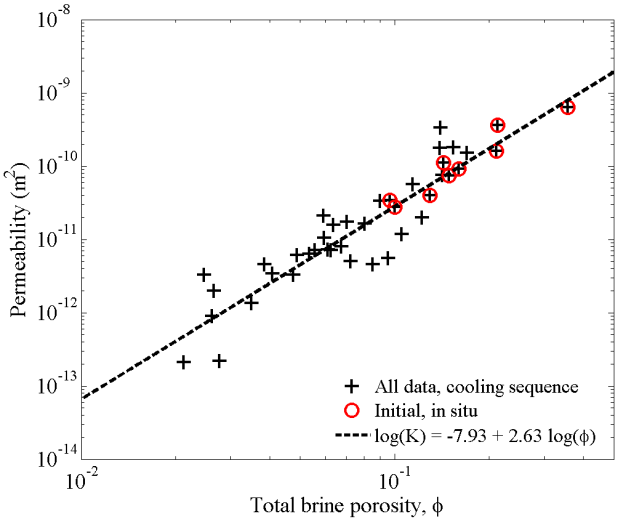

Figure 8: Relationship of simulated vertical permeability K and the total brine porosity ϕ. The red symbols are from the core centrifuged at *in situ* temperatures, while the crosses refer to all cores cooled in the lab, resulting in lowered ϕ.

While in the latter figure the lowest ϕ values of the field core samples are about 4%, values as low as 2% are determined for the subsamples. This does not mean an inconsistency: As the imaged sample volume is roughly one tenth of the field sample volume, it reflects the internal variability. It is seen that the microscopic permeability computations support the finding from the macroscopic centrifuge data analysis: there is no indication of a threshold near 5% total brine porosity, as proposed on the basis of connectivity considerations of mostly laboratory samples (Golden et al., 2007). A more detailed analysis of this permeability-relationship and its dependence on pore sizes and networks is currently ongoing.

APPLICATION TO OIL-WATER DISPLACEMENT

To discuss the pore space and permeability results in terms of oil migration into sea ice we recall recent laboratory experiments, where oil did not penetrate further upward than 2-3 cm (Karlsson, 2009) and 5-10 cm (Otsuka et al., 2004) from its releases level, with an apparent limitation of its migration by a brine porosity of 10 % (Karlsson et al., 2011). As noted, the present simulations do not show a permeability threshold at or above 5 % brine porosity. Equation 2 may further be used to estimate the migration velocity due to Darcys law as $V\phi = K/\mu_n \Delta\rho g$, with gravity acceleration g, dynamic viscosity of oil μ_n and the difference $\Delta\rho = (\rho_w - \rho_n)$ between densities ρ_w and ρ_n of brine and oil. Taking typical values $\mu_n \approx 0.1$ mPas and 160 kg/m^3 for $\Delta\rho$, gives for $\phi = 0.05$ a migration of 0.15 m/day. This means that permeability alone was no limiting issue in the laboratory experiments of Otsuka et al. (2004), where observations of oil fractions were performed after 5-10 days[4]. We thus consider the penetration of (nonwetting) oil into sea ice filled with seawater or brine (wetting), and evaluate it in terms of the well known Young-Laplace equation for the capillary pressure P_c:

$$P_c = \sigma_{nw} cos(\theta) \left(\frac{1}{R_1} + \frac{1}{R_2} \right), \tag{3}$$

[4]Note that, even if effective relative oil permeabilities during the displament of brine by oil are expected to be lower (e.g. Bear, 1972; Sahimi, 1993), a reduction exceeding a factor of 10 is unlikely for brine saturation above 50%, as in the expertiments.

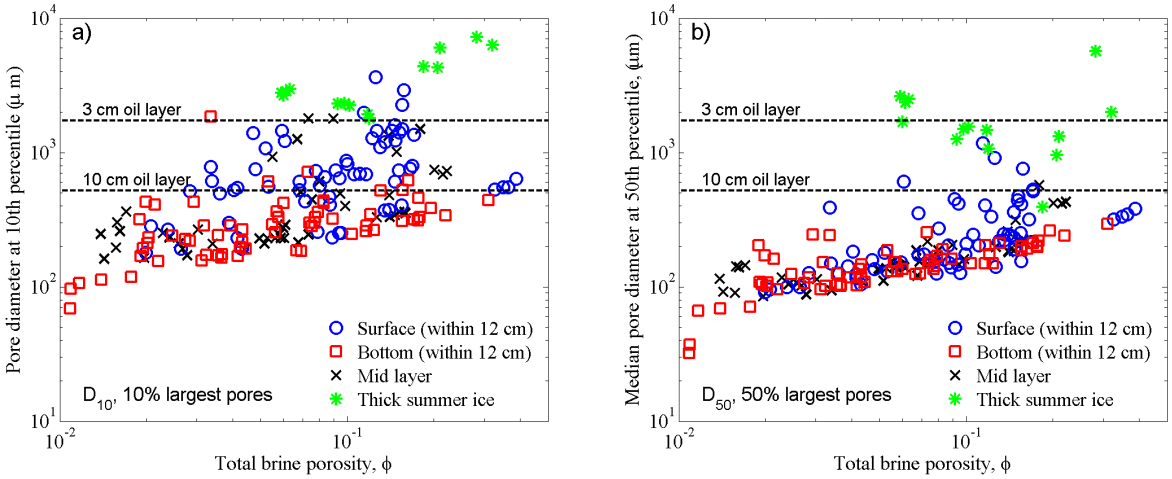

Figure 9: a) Pore diameter D_{10} dividing the largest 10th percentile (by volume) of the pore space distribution in dependence on total brine porosity. Surface, mid part and bottom samples of the 35 cm thick young ice are distinguished in the legend. The results are contrasted with D_{10} obtained for a sample 40 cm from the bottom of older summer ice (green stars). The horizontal lines represent the critical entrance capillary diameter for oil drainage for pressures corresponding to heights of 3 and 10 cm. b) The median pore diameter D_{50} of the pore space distribution. Note that a 10 centimeter oil layer in under ice pools may be expected for 1 m thick ice (see text).

where R_1 and R_2 are the principle radii of curvature, σ_{nw} is the oil-water surface tension and θ the oil-ice contact angle. Simplifying for capillaries with circular cross section the right hand factor becomes $2/R$. If P_c is assumed to be related to the buoyancy of oil in water in a capillary of height H, it equals

$$H = \frac{2\sigma_{nw} cos(\theta)}{g\Delta\rho R}. \tag{4}$$

Inserting characteristic properties for crude oil of $\sigma_{nw} \approx 0.02$ J/m^2 (Malcolm and Dutton, 1979) and a density difference $\Delta\rho \approx 160$ kg/m^3 of crude oil and water, yields the approximate relationship $H \approx 2.6 \times 10^{-5}/R$, where both H and R are given in meters.

According to Equation (4), when a 5 mm oil layer is released below the ice, as typical for the mentioned experiments (I and II, see introduction), the oil would not enter channels that have a diameter less than 5.2 mm. In practice, however, a second process will help to entrain oil into the ice. As the oil floats from below toward the bottom of sea ice, it there meets a low porosity skeletal layer of 2-3 cm thickness (Weeks, 2010). Convecting brine from this layer will be replaced by oil and create an effective oil layer of this thickness. A 3 cm layer then yields an entrance pressure that corresponds to a smaller pore diameter of about 1.7 mm. This process may explain that in the laboratory experiments of Karlsson (2009) oil was observed in brine channels of 1-2 mm width. But does this justify a constant brine porosity threshold for oil infiltration in general?

In Figure 9 we plot the median pore diameter (D_{50}) as well as the diameter D_{10}, such that the 10^{th} largest percentile of pores has larger diameters, for our ice samples against the total brine porosity. Red and blue symbols refer to near bottom and surface samples, respectively, black crosses to intermediate layers. In the same figures we indicate the critical pore sizes that result from two different entrance capillary pressures as two horizontal lines: The upper line corresponds to a 3 cm, the lower to an 10 cm oil layer. Looking first at D_{10} representing the largest pores in Figure 9a, it is seen that the range where the observations approach the 3 cm line from below, indeed is found near a porosity of 0.1. As the laboratory ice from Otsuka et al. (2004) is comparable (17 to 25 cm) to our field samples (33-36 cm) and both ice types have experienced a warming period, the comparison is not unreasonable.

Hence, while the data are scattered, the evaluation of the pore size distribution from field samples appears consistent with the porosity threshold indicated in the laboratory experiment. However, the main message of Figure 9 appears even more important: in the field, spilled oil

may be distributed below sea ice in pools that relate to fluctuations in its bottom topography, with a pool depth of roughly 10% of the level ice thickness (Dickins, 2011). This implies that, the thicker the ice, the higher the oil pressure/layer, and the lower the critical infiltration pore diameter and corresponding porosity threshold. The horizontal line for a 10 cm oil layer in Figure 9 is then representative for 1 meter thick ice in the field. Apparently this condition implies a large difference compared to the laboratory experiments in terms of forcing, indicating that the latter strongly underestimate the pore volume fractions that may be inflitrated by oil.

Furthermore, not only the maximum oil pool depths are expected to change with ice thickness and age, yet also the sea ice microstructure. To illustrate this we show pore space results from a sample ca 0.4 m from the bottom of 1.0 m thick summer first-year ice, as green stars in Figure 9. It is seen that for this ice the characteristic pore diameters are large enough that more than 50% of the pore space may be infiltrated by oil.

CONCLUSIONS

Comparing the present 3-d pore space analysis of young first-year ice with laboratory oil infiltration experiments we arrive at the following main conclusions:
1. Pores size characteristics/critical capillary pressures are consistent with an infiltration brine porosity threshold of 0.1-0.15 as pointed out on the basis of laboratory experiments (Karlsson et al., 2011; Petrich et al., 2013).
2. However, this threshold is not expected to apply generally under field conditions, where it will depend on the thickness of oil pools and the age of the ice.

These results are important for a revised evaluation of the oil uptake capacity of sea ice. A recent estimate of oil storage in the sea ice pore space was suggested by Petrich et al. (2013) to be 5 to 10 l/m^2, and thus roughly 20% of the range 10-60 l/m^2 that Fingas and Hollebone (2003) estimated for oil pooled and trapped within the bottom topography of sea ice. However, Petrich et al. (2013) obtained it by extrapolating the noted laboratory results. The present analysis indicates that sea ice in the field may take up significantly more oil, both due to a coarser microstructure, and in case of sufficiently large oil amounts and layer pressures from the bottom. While field observations appear limited, an indication may be obtained from the average weight percentage 4.5% of oil in warm sea ice obtained during (NORCOR, 1975). For 0.5 to 1 m thick ice this would yield a contribution of oil uptake that is comparable in magnitude to under-ice pooling.

To come up with quantitative estimates of oil infiltration and its ice thickness dependence, more microstructure observations are needed especially for sea ice of different age. As the drainage of oil is expected to be controlled by pore throats, it is likely that pore size distributions in Figure 9 overestimate the fraction of the pore space that may be infiltrated by oil. Furthermore, oil drainage into a water-wet porous medium as sea ice depends on other details of the pore space, e.g., 3-d connectivity, dead ends, brine saturation and boundary conditions (e.g. Bear, 1972; Sahimi, 1993). We are planning fluid simulations with the present samples to address the problem quantitatively.

The present work indicates that microstructural data are a very important issue to improve our understanding of oil-in-ice processes, in particular the predictability of horizontal transport and surfacing of oil that is spilled from below sea ice. We point out that these issues also are important for understanding the role of sea ice in climate (e.g., Hunke et al., 2011). The permeability of sea ice controls drainage of melted snow through the ice, exposing a brighter surface with higher albedo, while the process of desalination of sea ice also is related to its permeability (e.g., Notz and Worster, 2009; Weeks, 2010). Last but not least, fluid flow in sea ice also affects the sea ice microbiology, bio-geochemistry and the related ecosystems in high latitudes (Melnikov, 1997; Thomas and Dieckmann, 2003).

REFERENCES

Bear, J., 1972. Dynamics of fluids in porous media. Amer. Elsevier, reprinted by Dover Publ., 764 pp.

Cox, G. F. N., Weeks, W. F., 1983. Equations for determining the gas and brine volumes of sea ice samples during sampling and storage. J. Glaciol. 32, 371–375.

Dickins, D., 2011. Behavior of oil spills in ice and implications for Arctic spill response. In: Proceedings of the OTC Arctic Technology Conference, OTC 22126. pp. 1–15, Houston, Texas, USA.

Fingas, M. F., Hollebone, B. P., 2003. Review of behaviour of oil in freezing environments. Mar. Poll. Bulletin 47, 333–340.

Freitag, J., Wilhelms, F., Kipfstuhl, S., 2004. Microstructure-dependent densification of polar firn derived from X-ray microtomography. J. Glaciol. 50 (169), 243–259.

GeoDict, 2012. (Geometric material models and computational preDictions of material properties). Web: www.geodict.com.

Golden, K. M., Ackley, S. F., Lytle, V. I., 1998. The percolation phase transition in sea ice. Science 282, 2238–2241.

Golden, K. M., Heaton, H. E. A., Miner, J., Pringle, D. J., Zhu, J., 2007. Thermal evolution of permeability and microstructure in sea ice. Geophys. Res. Lett. 34, L16501.

Hunke, E. C., Notz, D., Turner, A. K., Vancoppenolle, M., 2011. The multiphase physics of sea ice: a review for model developers. The Cryosphere 5, 989–1009.

Karlsson, J., 2009. Oil movement in sea ice. Master's thesis, University of Copenhagen, enmark, 199pp.

Karlsson, J., Petrich, C., Eicken, H., 2011. Oil entrainment and migration in laboratory-grown saltwater ice. In: Proceedings of the 21st International Conference on Port and Ocean Engineering underArctic Conditions 10-14 July 2011. pp. 1–10, montreal, Canada. POAC11-186,.

Kawamura, T., 1988. Observations of the internal structure of sea ice by X Ray computed tomography. J. Geophys. Res. 93 (C3), 2343–2350.

Malcolm, J., Dutton, C., 1979. The interfacial tension and contact angle of crude oil under ice. Port and Ocean Engineering under Arctic Conditions , 771–778Norwegian Institute of Technology.

Martin, S., 1979. A field study of brine drainage and oil entrainment in first-year sea ice. J. Glaciol. 22 (88), 473–502.

Maus, S., Haase, S., Büttner, J., Huthwelker, T., Schwikowski, M., Vähätalo, A., Enzmann, F., 2011. Ion fractionation in young sea ice from Kongsfjorden, Svalbard. Annals Glaciol. 52 (57), 301–310.

Maus, S., Huthwelker, T., Enzmann, F., Miedaner, M. M., Stampanoni, M., Marone, F., Hutterli, M. A., Ammann, M., Hintermüller, C., Kersten, M., 2009. Synchrotron-based X-ray tomography: insights into sea ice microstructure. In: Leppäranta, M. (Ed.), Rep. Ser. Geophys., University of Helsinki. Vol. 61. 28-45.

Melnikov, I. A., 1997. The Arctic Sea Ice Ecosystem. Gordon and Breach, 204 pp.

NORCOR, 1975. The interaction of crude oil with Arctic sea ice. Vol. Technical Report No. 27 of Beaufort Sea Project. Department of Environment, Victoria, BC, Canada, 201 pp.

Notz, D., Worster, G., 2009. Desalination processes of sea ice revisited. J. Geophys. Res. 114, C05006.

Otsu, N., 1979. A threshold selection method from gray-level histograms. IEEE Transactions on Systems, Man and Cybernetics SMC-9 (1), 62–66.

Otsuka, N., Kondo, H., Saeki, H., 2004. Experimental study on the characteristics of oil ice sandwich. Proceedings of OCEANS '04 3, 1470–1475.

Petrich, C., Karlsson, J., Eicken, H., 2013. Porosity of growing sea ice and potential for oil entrainment. Cold Reg. Sci. Technol. .

Rogers, T., Walsh, J., Rupp, T., Brigham, L., Sfraga, M., 2013. Future arctic marine access: analysis and evaluation of observations, models, and projections of sea ice. The Cryosphere 7, 321–332.

Sahimi, M., 1993. Flow phenomena in rocks. Rev. of Mod. Phys. 65 (4), 1393–1534.

Schneebeli, M., Sokratov, S. A., 2004. Tomography of temperature gradient metamorphism of snow and associated changes in heat conductivity. Hydrol. Processes 18, 3655–3665.

Thomas, D., Dieckmann, G. S., 2003. Sea Ice: An Introduction to its Physics, Chemistry, Biology and Geology. Blackwell, 402 pp.

Weeks, W. F., 2010. On Sea Ice. University of Alaska Press.

Weissenberger, J., Dieckmann, G., Gradinger, R., Spindler, M., 1992. Sea ice: A cast technique to examine and analyze brine pockets and channel structure. Limnol. Ocean. 37 (1), 179–183.

Wolfe, L. S., Hoult, D. P., 1974. Effects of oil under sea ice. J. Glaciol. 13 (69), 473–488.